CFD study of Savonius wind turbine: 3D model validation and parametric analysis

G. Ferrari, D. Federici, P. Schito, F. Inzoli, R. Mereu *

Politecnico di Milano, Piazza Leonardo da Vinci 32, 20133, Milano, Italy

A CFD study is conducted in order to characterize the dynamic behavior of a Savonius vertical axis wind turbine. All simulations are executed using the open source code, OpenFOAM. Both two-dimensional and full three-dimensional cases have been investigated in order to provide a suitable tool for geometrical optimization of this rotor. Unsteady simulations are carried out at different tip speed ratio (TSR), varying angular speed of rotor at constant wind speed, using different one and two-equation URANS turbulence models and selecting the k − ω SST for the final analysis. The two-dimensional model was compared with experimental data available in literature and obtained from tests in wind tunnel. This simplified model shows an over-estimation of experimental data, reporting a maximum efficiency at TSR 1, 20% higher than experimental value. The results of 3D model are in good agreement with experiments with a peak of 0.202 at TSR 0.8 for a rotor with aspect ratio 1.1. The influence of the rotor height has been evaluated on flow dynamics of the turbine and its power coefficient.

1. Introduction

The importance of reducing GHG (greenhouse gases) leads to research more sustainable energy resource and to investigate more efficient technologies. Wind resource is one of the most exploited and in 2014 more than 50 GW have been installed [1]. Wind turbines are generally divided into two main categories: macro aeolian generation and micro aeolian generation. For the first purpose, horizontal axis machines have been developed, composed by a main rotor with air-foil blades and electric generator mounted at the top of a tower (50–150 m tall). While assuring high efficiency and high power, this type produces high noise and requires large space sites for installation. For micro generation, vertical axis devices could represent a valid alternative due to possibility of exploiting wind from variable direction without a complex and expensive control system and easy accessibility and maintenance of power train elements (installed near the ground). Considering this characteristic and low-noise, vertical axial turbines are suitable for urban context such as Savonius [2]. Design is simple and economically competitive and installation requires limited space and it is possible on the top of many buildings. The basic configuration of Savonius turbine is formed by two semicircular blades mounted around a central pole and arranged for creating S-shape. In order to improve the performance, several studies both experimental and numerical have been conducted changing scoop shape (Kamoji et al. [3] and Tian et al. [4]), number (Blackwell et al. [5] and Mahmoud et al. [6] and Damak [7]) and spacing (Blackwell et al. [5]) or adding end-plates (Mahmoud et al. [6] and Ushiyama et al. [8]), leading to relevant modification to original geometry. As this rotor remains a drag driven device, its typical working speed range is low, from 0.6 to 1.1 tip speed ratio (Shigetomi et al. [9]). The consequence is a lower output and a worse performance compared to horizontal axis wind turbines. Several aerodynamics theories have been applied to VAWT composed by aerfoils like Darrenius type (for example, chapter 5, Wilson [10]) but they are not suitable for Savonius configuration (Ushiyama et al. [8]). Despite the low output characteristics, it doesn't need a system for regulation of pitch or yaw and shows positive torque at every wind incident angle so that it is a self-starting wind turbine (Sivasegaram et al. [11]). The design is very simple and cheap. The installation requires low space and it is possible on the top of many buildings: Goh [12] finds the optimal installation position on a flat surface, studying the distance from an infinite-width forward facing step.

In literature, numerical studies are available exposing both 2D models (Kacprzak et al. [13], D'alessandro [14], Akwa [15] and Mohamed [16]) and 3D cases (Gunpta [17], Kang [18], Dobrev [19]

Article history:
Received 11 March 2016
Accepted 26 December 2016
Available online 4 January 2017

Keywords:
Vertical axis wind turbine (VAWT)
Savonius
CFD
Turbulence models
Aspect ratio
OpenFOAM

* Corresponding author.
E-mail address: riccardo.mereu@polimi.it (R. Mereu).

Published Journal Article available at: http://dx.doi.org/10.1016/j.renene.2016.12.077

and Jaohindy [20]). Dobrev et al. [19] offers also a an application case of RANS and DES models. Roy et al. [21] and Krysinski [22]. Nasef et al. [23] studied the sensitivity in the static and dynamic performances of a two bucket Savonius rotor as function of the RANS model. He concluded that $k-\omega$ SST is suitable for simulating the flow pattern around the Savonius rotor than other models for both stationary and rotating cases.

In this article, using the open source code OpenFOAM, unsteady 2D and 3D simulations are reported analysing the aerodynamic performance and forces acting on this type of rotor. This work is divided in three parts: grid and case set-up; validation of the code; aspect ratio influence. The first section discusses the CFD solver settings and the work on the grid, based on 2D case because of reduced time calculation. In the second part, a complete 3D case is developed in order to validate results from computational model using experimental data. A 2D/3D comparison is proposed for clarifying limits and capabilities of 2D model. Finally, efficiency of turbines with different height, keeping fixed the cross-section geometry is analysed using the 3D model.

2. Benchmark

In order to validate numerical results, Sandia laboratories data [5] has been taken as benchmark. Blackwell et al. (1977) carried out an in depth investigation of low-speed wind tunnel testing of Savonius type rotors of two/three stages and two/three blades at different Reynolds numbers whilst measuring variables: torque, RPM and tunnel conditions. Blackwell presents data in the form of power and torque coefficients and as a function of tip speed ratio (or angular position for static starting torques); it was concluded that increasing Reynolds number and/or aspect ratio improves the performance.

In this work, static turbine performance are neglected, focusing on complete rotating machine characteristic curve. All simulation have been conducted with a Reynolds number based on turbine diameter (D_t) and bulk velocity (U_{inf}) equal to $4.32 \cdot 10^5$, the same used in Sandia tests.

$$Re = \frac{D_t\, U_{inf}}{\nu} \tag{1}$$

3. Computational description

3.1. Savonius geometry

As displayed in Fig. 1, the studied Savonius turbine is composed of two semicircular blades with diameter, d, and height, H, divided by a gap, o. This space is reported as overlap ratio, OR, defined by o/d; in this work all rotors have overlap ratio equal to 0.2. The diameter of turbine is 0.9023 m while the circular end plates are characterized by 1 m diameter. Many authors reports a ratio 1.1 between turbine diameter and disk dimension as optimum configuration (Sivasegaram et al. [24]). Four different configurations have been investigated, keeping fixed the cross section parameters, and varying only the height of cups. Table 1 below reports the geometrical parameters.

$$AR = \frac{H}{D_t} \tag{2}$$

3.2. Performance parameters

Dynamic torque coefficient C_m and power coefficient C_p generated by the Savonius rotors are monitored and calculated as following:

$$Cm = \frac{M}{\frac{1}{4}\rho U_{inf}^2 D_t};\; Cp = \frac{P}{\frac{1}{2}\rho A U_{inf}^3} \tag{3}$$

where A is the frontal area of the rotor, D is the diameter and U_{inf} is the free stream velocity of the wind corrected with the blockage factor (only in 3D cases). M is the dynamic torque and P is the power produced. It was also monitored the coefficients of longitudinal drag C_d, lateral lift C_l and the equivalent force C_{res}.

$$C_d = \frac{Lift}{\frac{1}{2}\rho A U_{inf}^2};\; C_l = \frac{Drag}{\frac{1}{2}\rho A U_{inf}^2};\; Cres = \sqrt{C_d^2 + C_l^2} \tag{4}$$

The power coefficient, C_p, is used to identify the grid convergence (next paragraph) and to evaluate the wind turbine performance (efficiency). This coefficient represents the fraction of extracted power from the total available in free stream of air flow at undisturbed velocity U_{inf} that runs through the projected area of rotor at the flow direction. Simulations have been conducted at different angular rotor speed, expressed by following a dimensional number:

$$TSR = \frac{\pi\, RPM\, D_t}{60\, U_{inf}} \tag{5}$$

3.3. Numerical models and methods

Turbulent flow is modelled through URANS models using a Reynolds-Averaged version of continuity and Navier-Stokes equations and transport equations for turbulence quantities. The modeling based on this technique requires the use of modified transport equation for mass, momentum and, when present, energy and the use of specific numerical methods for their temporal and spatial discretization deeply explained in Ref. [25]. In this study three well-known one and two-equations URANS models are evaluated: Spalart-Almaras [26], Realizable $k-\varepsilon$ [27], and $k-\omega$ SST (Menters Shear Stress Transport [28]). Only dynamic simulations have been conducted. The dynamic motion fixes the angular rotational speed despite of the forces acting on the blades. This approach doesn't resolve initial start-up period but allows fast generation of efficiency data. The solver is transient for incompressible flow of Newtonian fluids on a moving mesh using the PIMPLE (merged PISO-SIMPLE) algorithm. For all simulation presented in this work the boundary conditions have been set as follows. At the inlet, wind velocity is set equal to 7 m/s and zero gradient condition on pressure. At the outlet, pressure is fixed to zero and velocity gradient is zero. Lateral, top and bottom boundaries are set to symmetry condition (only in the 2D case, top and bottom patches are set to the empty boundary condition). On turbine surfaces, blade and end plates (in 3D simulations), a no slip condition has been applied on velocity and zero gradient on pressure. The use of a $k-\omega$ SST formulation allows the description of all wall boundaries through the viscous sub-layer approach, without any extra wall functions. This is obtained with the use of several layers on blades in order to keep y^+ below 1. Mesh characteristics will be further discussed below. The physical (U_{inf}, p) and turbulence properties on the entire domain have been initialized with the same values of inlet boundary condition. This choice leads to an

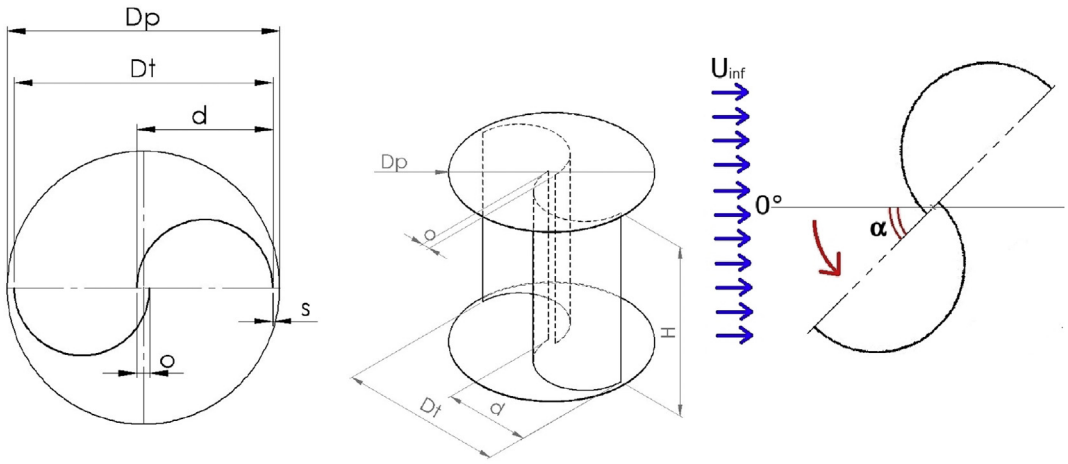

(a) Cross Section (b) 3D view (c) Cross Section

Fig. 1. Convention for rotation.

Table 1
Geometric parameters of studied configurations.

	Rotor A	Rotor B	Rotor C	Rotor D
H	0.5	0.7	1	1.5
Dt	0.9023	0.9023	0.9023	0.9023
d	0.5	0.5	0.5	0.5
s	0.002	0.002	0.002	0.002
AR	0.58	0.78	1.11	1.66
Re	$4.32{*}10^5$	$4.32{*}10^5$	$4.32{*}10^5$	$4.32{*}10^5$

initial transient period during first revolutions. Data are taken when efficiency (Cp) is constant and have been averaged on 4 revolutions.

Using Equation (6), inlet k value is computed imposing the turbulent intensity equal to 1.4% as reported for wind tunnel experiment [5].

$$k = \frac{3}{2}\left(U_{inf} I\right)^2 \tag{6}$$

$$\omega = C_\mu^{\frac{3}{4}} \frac{k^{\frac{1}{2}}}{l} \tag{7}$$

where C_μ is 0.09 and l is 0.07 times the hydraulic diameter of wind tunnel, described below. Average Courant number is maintained below 1 in all simulations in order to keep good stability and accuracy of the method; the maximum value is below 10, recorded in the cells on blade tips due to small dimension and the frontal impact of the wind during the revolution. Time step is kept fixed during simulation but adapted to different tip speed ratio conditions. This settings have been chosen in order to generate reliable results limiting the computational demand of the case. Even if LES simulation can give more accurate fluid dynamic description, it would require too high resources, not acceptable for the purpose of the study.

3.4. Grid convergence analysis

A GCI analysis and mesh optimization have been carried for 2D configuration representing the cross median section of the rotor. Initially a grid convergence analysis has been carried out for obtaining a solution not affected by discretization errors, then an optimization of the grid zones has been realized in order to maintain the same results while reducing the number of cells. The rectangular domain shown in Fig. 2 is divided into two zones: a rotating circle including the rotor (a); a fixed region surrounding it (b). The coupling is realized by AMI (Arbitrary Mesh Interface). Each face accepts contributions from partially overlapping faces from the neighbour patch, with the weights defining the contribution as a fraction of the intersecting areas. For each face, the sum of the weights (contributions) should equal 1. Conservation errors are below 1e-5, in this case. The moving zone has 2 D_t radius. All 2D domain extends 9 D_t upstream, 17 D_t downstream the rotor and 6 D_t on later side. An analysis on later domain size has been conducted and the results are shown in Fig. 3. The sensitivity analysis demonstrates that a domain of 12 D_t is appropriate for this study showing a difference with the domain of 20 D_t lower 1%. As shown in Table 2, three grids have been realized, refining every time all the cells by splitting each of them in four elements and maintaining constant the dimension of layer over blade surfaces in order to keep y^+ under 1. In Fig. 4, the results enlighten that an asymptote has been reached with "medium" and "fine" mesh. "medium" grid represents the right trade-off between accuracy and number of cells. The discretization error, generated by this grid, on torque coefficient is 0.03% compared to a mesh, composed by almost four times the elements number.

In the second phase, the morphology of refinement regions has been changed in order to limit the number of cells while maintaining a good accuracy of results. Each blade has been split into

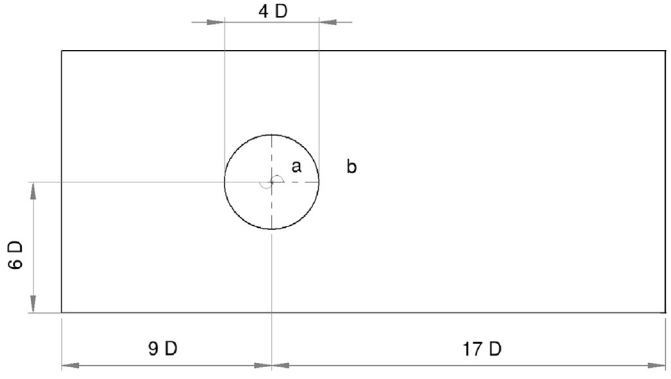

Fig. 2. 2D domain.

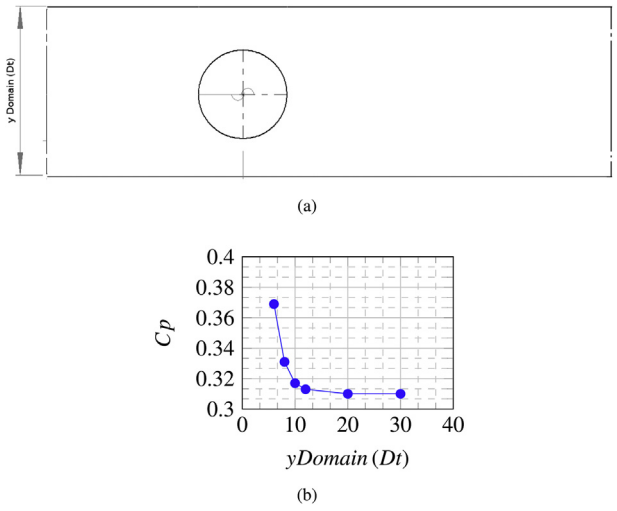

Fig. 3. Cp coefficient as function of domain lateral size.

three parts, from apex to central zone. This allowed to keep thinner cells on the edge, crucial zone for vortex generation, and reducing the number of cells in the central zone. In the rest of domain, a gradual transition from zone around the rotor to boundaries has been constructed. In Fig. 5 the final result of this effort can be observed. This work was necessary for the subsequent 3D simulations. Extruding the first "medium" mesh in third dimensions would generate a too heavy case. The final grid consists of 50960 cells assuring a performance difference with "medium" grid below 1% at all TSR. This result was satisfactory, considering the calculation time saving due to 70% less cells. Final grid characteristic and data comparison can be seen in Table 3.

3.5. 3D computational mesh

The mesh has been realized using open-source utilities implemented in OpenFOAM 2.3.x: blockMesh and snappyHexMesh. After creating a background hexahedral grid by the first tool, the mesh is refined in the region around the rotor and downstream it (see Table 4). The grid discretization for rotor cross section is the same obtained by 2D grid analysis while a grading system has been applied for obtaining thinner cells near end-plates. The entire surface of blades (100%) is covered with a 8 layers. The end-plates don't have layers because of limiting the number of elements and y^+ being in range from 50 to 150. In this part of the domain, a logarithmic law of the wall is applied.

3.6. 3D data deduction

Regarding 3D simulation, the computational domain extends 8 m upstream and 15 m downstream the rotor with a cross section is 4.6 m high and 6.1 m width. These dimensions are the same of Sandia wind tunnel test [5]. The rotor occupies a relevant portion of cross area so the wind speed is accelerated because of reduced available zone. The free-stream wind speed is corrected with a

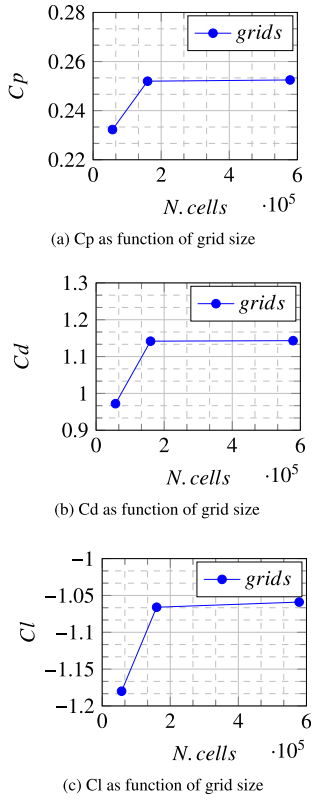

Fig. 4. Grid analysis.

blockage factor λ, as done for experimental data by Blackwell. Pope and Harper correlation is valid in this case (Ross [29]) and is defined as following:

$$U_{inf} = U_{FS}\,(1+\lambda);\ \lambda = \frac{D_t\,H}{4A_{WT}} \tag{8}$$

where U_{FS} is the free stream velocity of the wind and A_{WT} is the frontal area of the wind tunnel. 3D model data are corrected with the correlation expressed, while for 2D model uncorrected free-stream velocity is used.

4. Results and discussion

In the previous paragraphs a first phase of the numerical approach validation procedure [30] has been presented with the GCI sensitivity analysis. In order to complete the validation process further sensitivity analysis and comparisons with experimental data are reported here. In this section results of 3D case with AR 1.11 (Rotor C) are reported in detail for three different angular speeds. Starting from data average of a rotation, a comparison between CFD and wind tunnel is proposed. Moreover, polar charts for torque, lift and drag are displayed to give a complete overview of characteristics of this machine during rotation. The second paragraph is dedicated to analyze the difference between 3D and 2D model,

Table 2
Grid analysis.

Name	Cells	TSR	Cm	Cp	Err.	Cd	Err.	Cl	Err.
Fine	578575	0.81	0.311	0.252	–	1.143	–	−1.059	–
Medium	159999	0.81	0.311	0.252	0.03%	1.142	0.08%	−1.066	0.66%
Coarse	57000	0.81	0.287	0.232	7.94%	0.972	14.9%	−1.180	3.87%

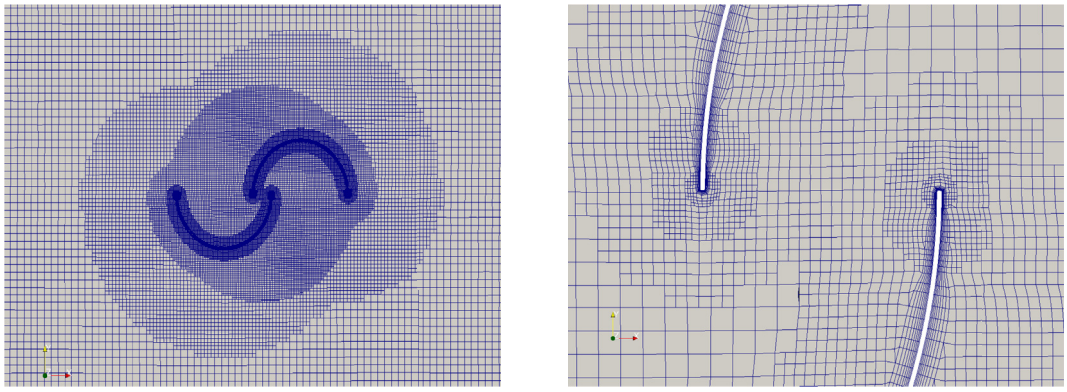

(a) *Zone near rotor.* (b) *Gap between blades.*

Fig. 5. Final 2D mesh.

Table 3
Comparison between "medium" and final 2D grid.

TSR	Cm *Medium* grid	Cm final grid	Error %
0.58	0.380	0.377	−0.79
0.81	0.311	0.313	0.61
1.01	0.264	0.263	−0.38

Table 4
Number of cells and blockage factor of four grids.

AR	Number of cells [10^6]	Blockage factor ε %
0.554	4.654	0.39
0.776	5.805	0.55
1.108	7.251	0.78
1.664	11.405	1.17

enlighting errors and positive aspects of the latter. Simulations have been conducted with uniform incident wind speed in order to reproduce the same condition of wind tunnel tests and validate the case. Real wind characteristics and fluctuations in speed and directions could influence the performance requiring a specific investigation of such conditions.

Table 5
3D model data at different TSR.

TSR	Cd	Cl	Cres	Cm	Cp	Error % C_p
0.576	1.136	−0.733	1.135	0.323	0.186	7.81
0.804	1.109	−0.798	1.367	0.251	0.202	8.76
1.002	1.097	−0.853	1.476	0.187	0.188	9.02

4.1. Models validation

As visible from the Fig. 6 (a), the 3D model is able to obtain power coefficient values within the band of uncertainty of the instruments used in experimental research, at all tested TSR. As shown, the three-dimensional simulation has solved the problems that the two dimensional approximation presents at high TSR. In this case, the shape of the curve is replicated with an average underestimation around 8%. In Table 5, the integral values of the most important parameters of the rotor are reported. The last column is relative percentage error of the power coefficient extracted with the 3D numerical model compared to the experimental one. There are no real data on drag and lift. The discrepancy in the efficiency of the rotor from wind tunnel results is aligned with the values reported in the literature by other authors using 3D URANS approach and with an error lower than experimental uncertainty (Zhao [31], Dobrev [19]).

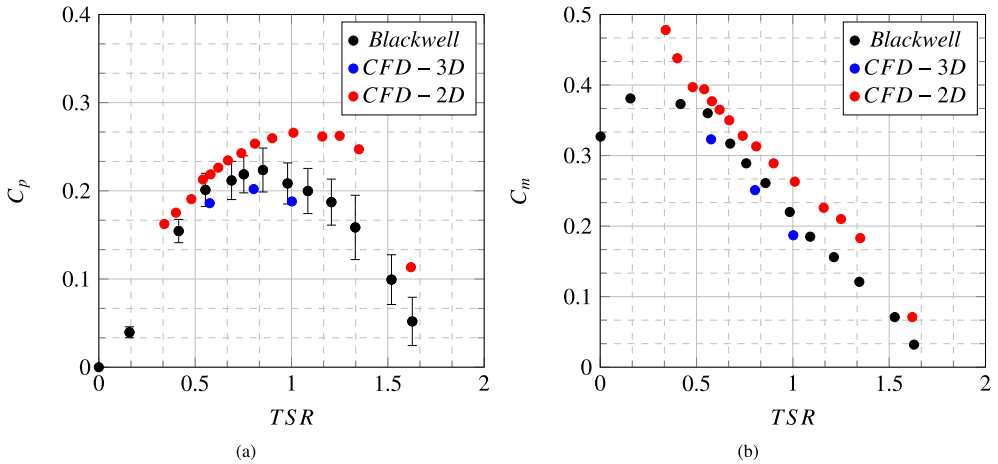

Fig. 6. (a) Cp obtained by 2D, 3D (H = 1m) computational models and experimental data from Blackwell. (b) Cm obtained by 2D, 3D computational models and experimental data from Blackwell.

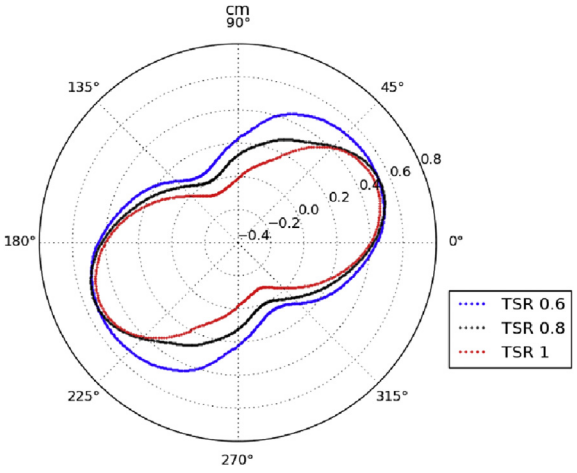

Fig. 7. Cm obtained by 3D (H = 1m) computational models at different TSR.

Fig. 7 shows a polar diagram that compares the rotor torque coefficients at the three TSR simulated. The maximum value stays essentially unmodified at the various operating conditions and stood slightly above 0.5. Even the angular position in which the rotor has the maximum torque remains stable around the 30°. The main differences are noticed during the rest of the rotation: at lower angular speed, values remain high for a wide range of positions contrary to operating points with higher rotational speeds.

In Fig. 8, the coefficients of drag and lift respectively are reported in a complete revolution of the rotor, gathering the three TSR conditions. Starting from the coefficient of drag (Fig. 8 (a)), punctual differences are observed between the various curves; also mutual position shifts during revolution. This leads the integral value change lightly between the different operating conditions. The maximum value is close to angle 60°. Focusing on C_l (Fig. 8 (b)), it is shown how the curve of the lowest TSR is always lower than the other. This confirms what reported in literature on the importance of longitudinal forces for the Savonius rotor: at high speed rotations (in reference to this type of turbine), the transverse thrusts are not negligible in the calculation of the generation of the torque. The peak value is calculated when the rotor is in position close to 20°-25° (slightly lower for the condition TSR 1.0).

Table 6
Comparison between data obtained by 2D and 3D computational models at different TSR.

	2D	3D	Difference %
(a) TSR 0.58			
C_d	1.157	1.136	1.82
C_l	−0.907	−0.733	19.2
C_m	0.377	0.323	14.32
C_p	0.219	0.186	15.07
(b) TSR 0.81			
C_d	1.139	1.109	2.63
C_l	−1.052	−0.798	24.14
C_m	0.313	0.251	19.8
C_p	0.254	0.202	20.47
(c) TSR 1.01			
C_d	1.123	1.097	2.31
C_l	−1.187	−0.853	28.14
C_m	0.263	0.187	28.90
C_p	0.266	0.188	29.32

4.2. 2Dvs3D modeling comparison

Table 6 shows the integral values obtained from the model two-dimensional and three-dimensional at the same operating conditions. It is possible to observe that the difference of the torque coefficient increases between the two models with the TSR, from a 14% at TSR to 0.58 to a 29% TSR to 1.01. The peak of 2D model at TSR 1.01 is reported by other author (Mohamed [16]). Attention must be paid to the fact that the greater discrepancy lays in the lift coefficient, that is the transverse forces the turbine experiences. The exact opposite occurs for drag, whose variation is contained below the 3% between the two models.

The differences between the two models are evident from the polar plots shown in Figs. 9–11. Generally, at all TSR, the two-dimensional model has clearly a widespread overestimation of the torque that is developed on the blades. Each angular speed shows its own peculiarities. At TSR 0.58 (Fig. 9 (a)), the two-dimensional simulation has two peaks of torque at angles in the neighbourhood of 30°, a phenomenon not present in the full three-dimensional model. Both at the minimum point (angle 120°), the torque is higher than in the two-dimensional model. Regarding the other two rotation speeds (Figs. 10 and 11), the rotor has a single peak in the two-dimensional torque but rather anticipated. In fact, it occurs in rotor positions around 20°-25°, compared to 30°-35° of

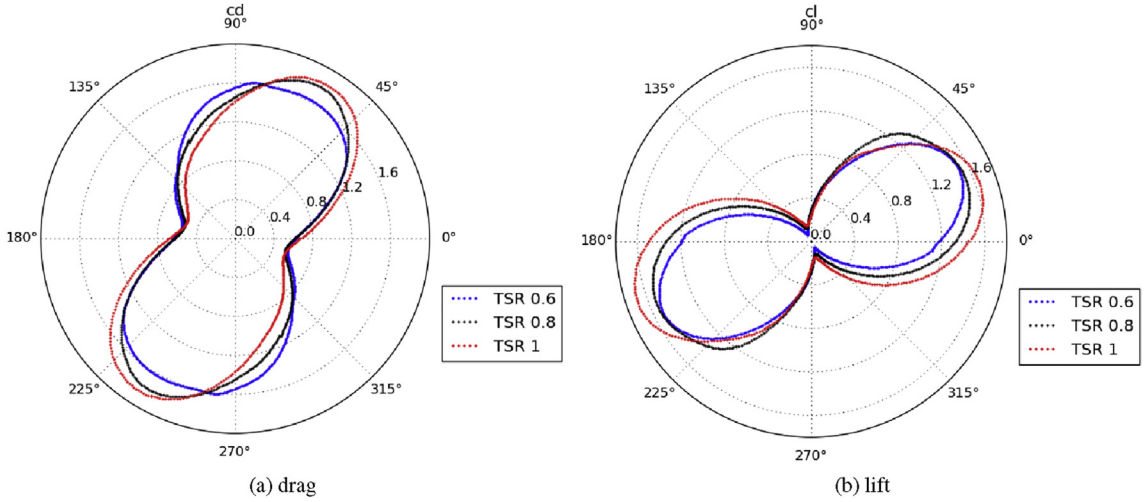

(a) drag (b) lift

Fig. 8. Cd and Cl coefficients obtained by 3D (H = 1m) computational models at different TSR.

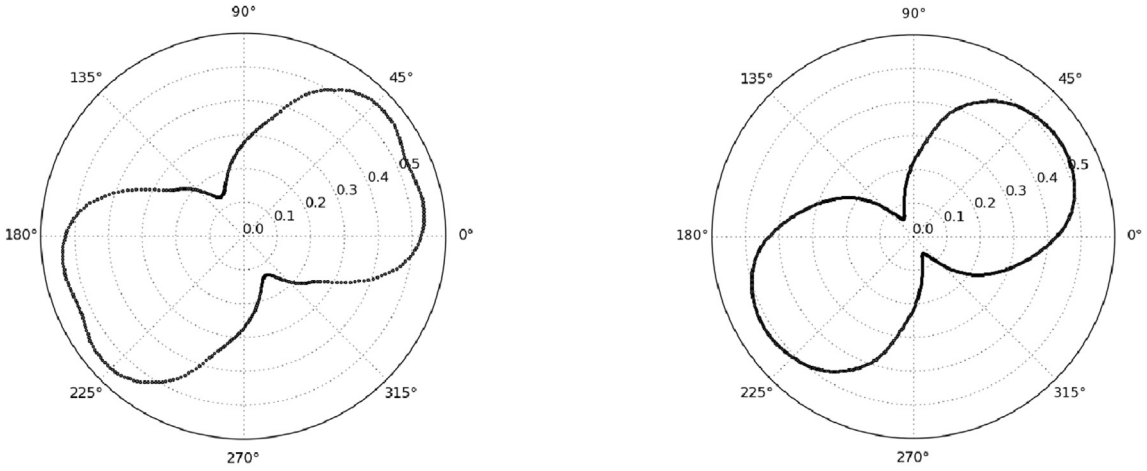

(a) C_m 2D model (b) C_m 3D model (H = 1m)

Fig. 9. Polar charts at TSR 0.58.

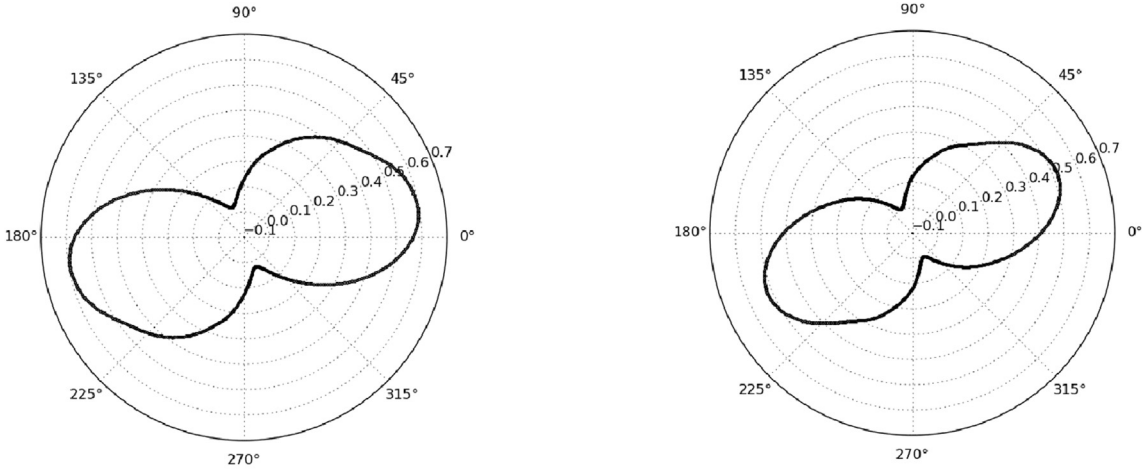

(a) C_m 2D model (b) C_m 3D model (H = 1m)

Fig. 10. Polar charts at TSR 0.81.

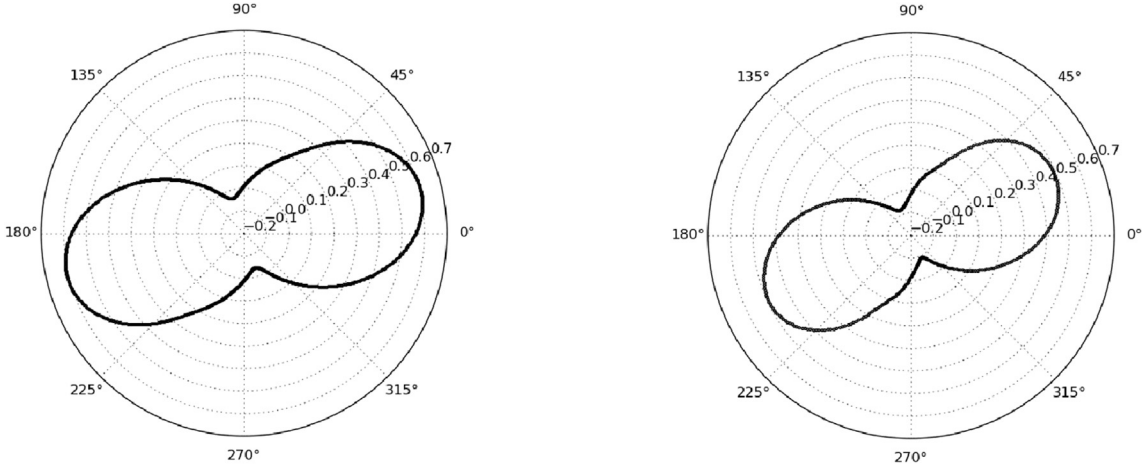

(a) C_m 2D model (b) C_m 3D model (H = 1m)

Fig. 11. Polar charts at TSR 1.01.

turbine with height 1 m. In these conditions of operation however, the minimum moment of the two models is almost the same; it lies close to the 120° when the returning blade deviates free stream wind preventing the direct impact on driving blade.

4.3. Turbulence models sensitivity analysis

A further sensitivity analysis is carried out comparing the $k-\omega$ SST model used in the GCI and 2Dvs3D modeling analysis with other well-known URANS turbulence models used for external aerodynamic: one-equation Spalart-Allmaras and two-equation Realizable $k-\varepsilon$ models. Pressure and momentum coefficients at TSR = 0.81 are compared showing a general underestimation of both coefficient with respect to experimental data. Spalart-Allmaras and Realizable $k-\varepsilon$ underestimate $k-\omega$ SST results of 10% and experimental data of 20%. Polar charts of torque C_m, drag Cd, lift Cl and force C_{res} coefficients of Realizable $k-\varepsilon$ model are reported in Fig. 12.

5. Aspect ratio variation

In this section, it is proposed a comparison among the four rotor with different aspect ratio (geometric parameters described in Fig. 1). These 3D simulations have been conducted at TSR 0.81.

As can be observed from the Fig. 13 (a), a rotor with lower height provides worse performance, considering that rotor A, 0.5 m tall, has power coefficient equal to 0.179. In percentage terms compared to the turbine with AR 1.01, this is equal to a efficiency loss superior to 11%. The same graph suggests the presence of an asymptote in performance curve; as the height increases, the marginal gain is continuously decreasing.

The efficiency indicated by the two-dimensional model remains distant, symptom that three-dimensional effects and losses due to edge effect remain important. Table 7 provides additional information for the study of machine behaviour. The coefficient of drag has a decreasing trend for higher aspect ratio, the variation between the two extreme configurations is about 8.3%; the lift has the opposite tendency with a difference of 37.9%. Consistently the 2D can be seen as infinite AR machine, characterized by higher lift coefficient. A rotor with greater height approaches better this approximation, confirming also the role of end plates play for improving the two-dimensionality of the flows, preventing the passage between the convex and concave side of the blades at the end of the same (Ushiyama et al. [8]). The two extremes are

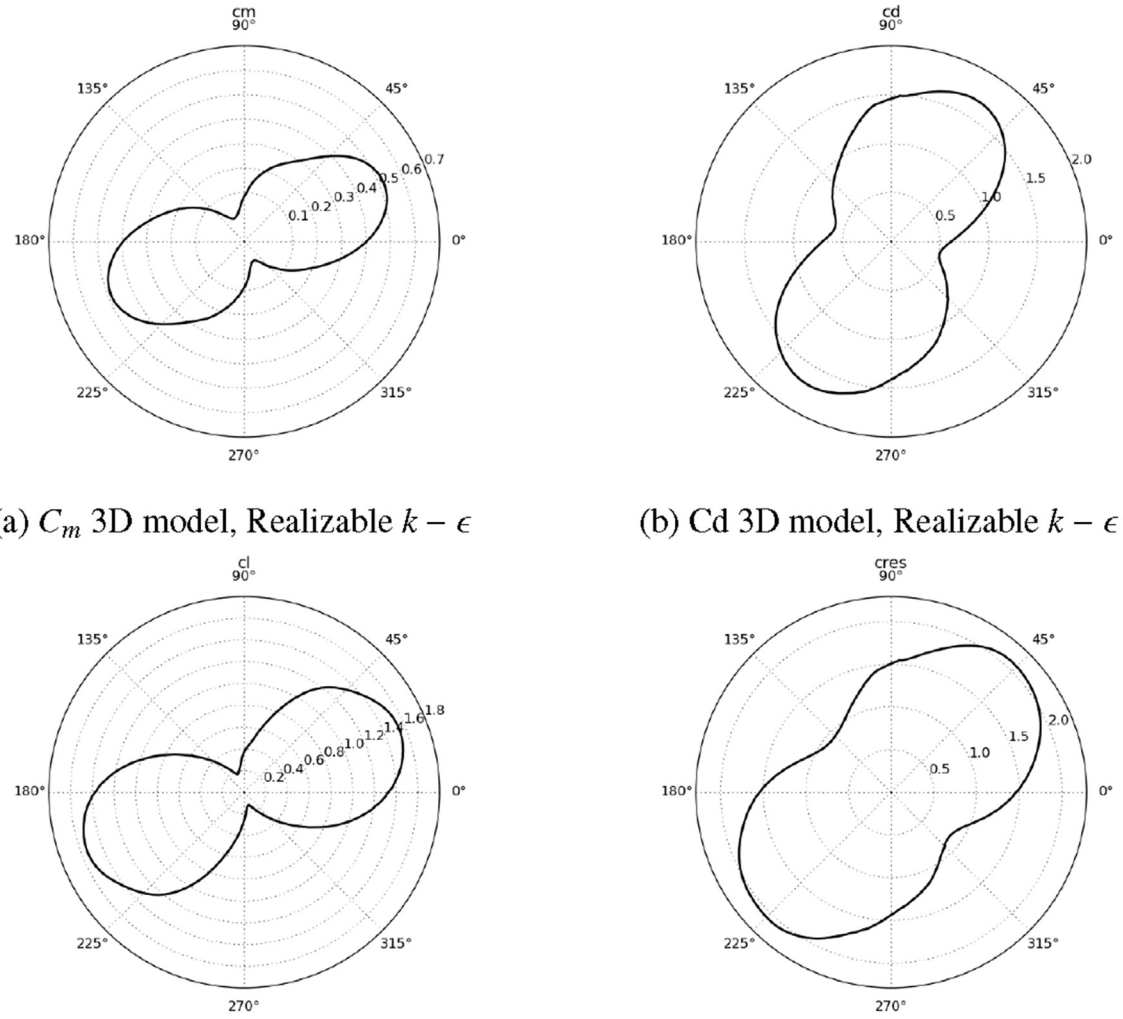

(a) C_m 3D model, Realizable $k-\epsilon$

(b) Cd 3D model, Realizable $k-\epsilon$

(c) Cl 3D model, Realizable $k-\epsilon$

(d) C_{res} 3D model, Realizable $k-\epsilon$

Fig. 12. Polar charts at TSR 0.81 of 3D Realizable $k-\varepsilon$.

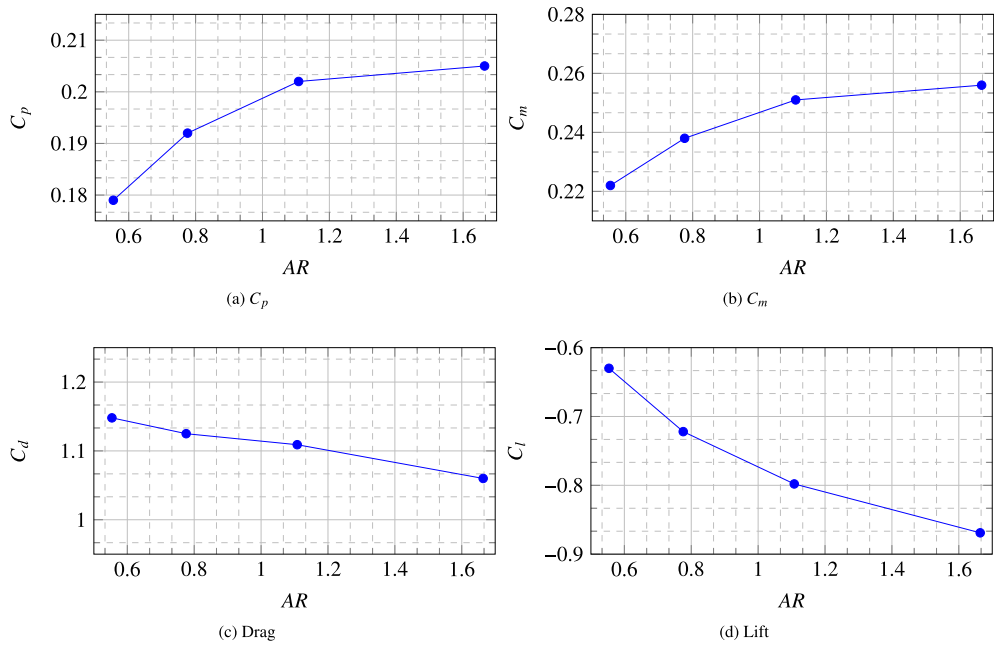

(a) C_p (b) C_m (c) Drag (d) Lift

Fig. 13. Drag, Lift, C_{res}, C_m as function of TSR.

Table 7
Results as function of aspect ratio.

AR	TSR	Cd	Cl	Cm	Cp	Variation % Cp
0.554	0.807	1.148	−0.630	0.222	0.179	−11.14
0.776	0.806	1.125	−0.722	0.238	0.192	−4.99
1.108	0.804	1.109	−0.798	0.251	0.202	–
1.664	0.801	1.060	−0.869	0.256	0.205	1.56

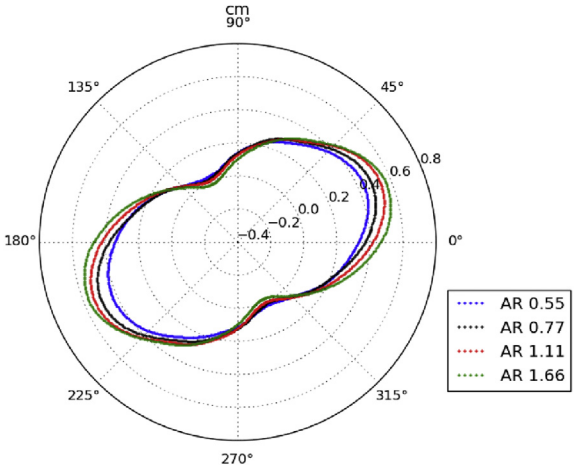

Fig. 14. Polar charts of Cm as function of AR.

characterized by C_{res} that differs by 5%.

Looking at the polar diagram in Fig. 14, the point of maximum torque is around the 30° for all configurations while the minimum stabilizes around 120°. The absolute value of the maximum point increases with growing aspect ratio; the main difference is visible for lower rotor while it fades between the two highest. On the contrary, the minimum value is greater for the rotor with aspect ratio 0.55; turbine D begins to show also points with resultant torque slightly negative.

Fig. 15 reports the torque coefficient that every cup generates, in four different aspect ratio. The single blade has the point of maximum positive torque at angular values slightly higher than the maximum point of the rotor as a whole. In this position of the machine (angle 30°), two main phenomena are important: for greater heights pushing blade increases its effectiveness, while the dragged one offers less resistance torque to the rotor. Turning instead to the minimum point, the relations are reversed, with the advancing blade of smaller turbine that provides greater torque.

In the polar diagram 16 (b), it is clear how the lift force undergoes a major change for the different rotors, increasing in magnitude at all angles for turbines with aspect ratio higher. This confirms the integral data seen in Table 7. For completeness, also shows the results of the coefficient of drag of the rotor, Fig. 16 (a), which on the contrary undergoes a slight drop for rotors highest.

5.1. Local forces

In Fig. 17, a study is reported about torque coefficient at different position along the rotation axis of the rotor. Each point is the mean on a thin stripe of 2 mm with the rotor in position 36°. All numbers are instantaneous values and not a mean on entire rotation. An evolution is observed from model A to D. For the lowest rotor, there is a parabolic curve between the two end disks. The flux is not fully developed and independent from end-disk effect. Passing through different step, the rotor with AR 1.66 is characterized by a flat central zone where torque is substantially stable. Near end plates, the effect of velocity deceleration on these disks causes a reduced thrust on blades and low torque.

The graphs in Fig. 18 shows the main parameters coefficient values on the median plane with the average value of all height, calculated in the same rotor angular position of the preceding paragraph. The trends are not uniform for the four parameters measured but consistent with the assertion done about 2D and 3D models. The coefficient of drag of the turbine has smaller variation compared to the other parameters (Fig. 18-(a)). At the same time, difference between mean and medium value is little. The insensitivity of the longitudinal forces on the turbine to the different

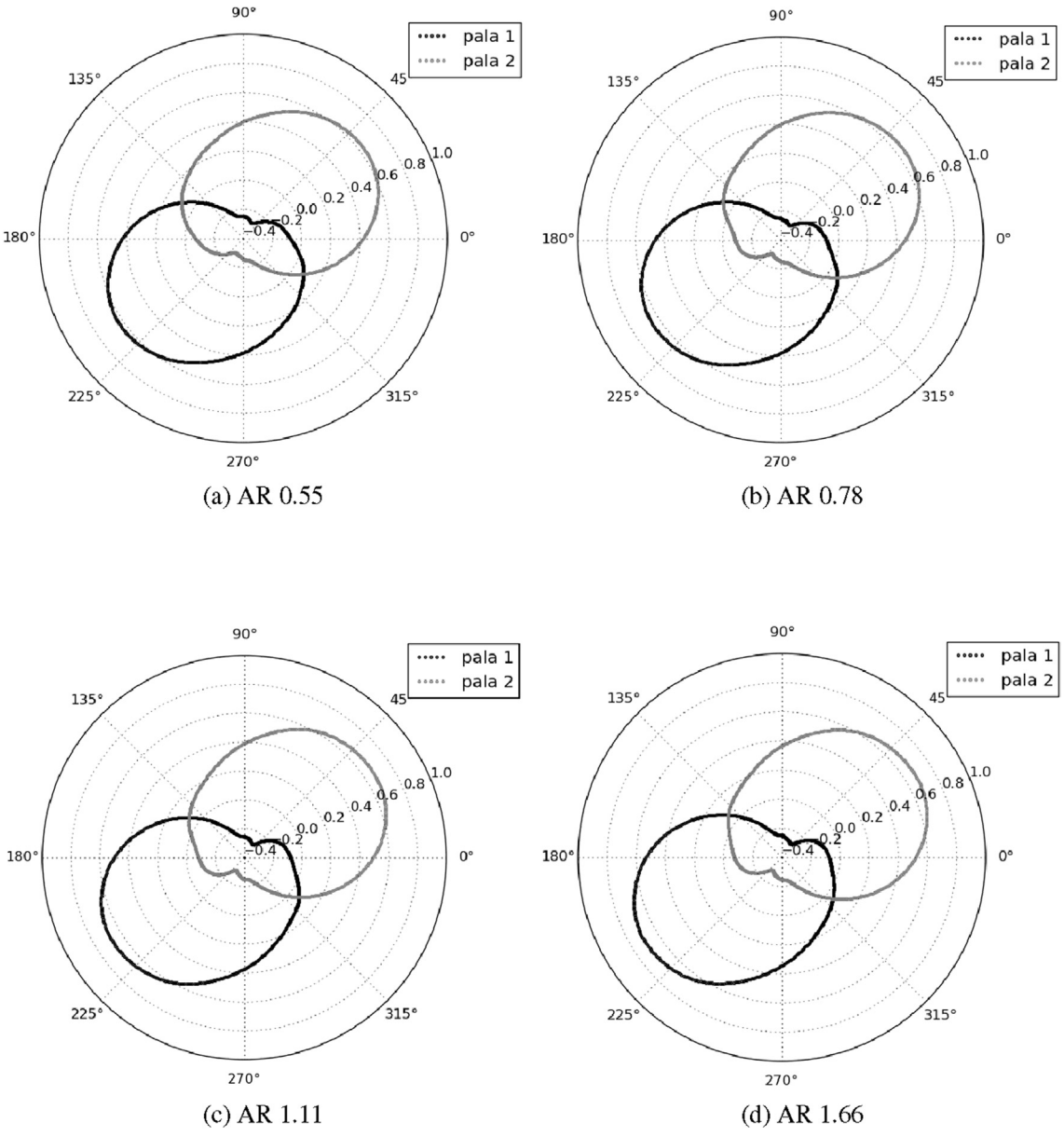

Fig. 15. Polar chars of blade Cm as function of AR.

parameters has already been emphasized several times during this discussion. The curve seems linear, decreasing for taller rotors. On the contrary (Fig. 18-(b)), the lift changes heavily in different geometries; its value in the median plane increases with higher aspect ratio. This is connected to the two-dimensional flow characteristic in the mid-line that is more relevant for a high rotors. In fact, the 2D model is distinguished by the high lateral forces that are detected on the rotor. It is not possible to draw an asymptote for this coefficient because the marginal changing does not seem to decrease as well as the difference between the median and the average. Turning to the torque generated (Fig. 18 (d)), Turbines C and D have a very similar peak efficiency in the median plane while they differ in the average value. The reason is the penalty of region close to the plates that has bigger weight for a lower rotor. The other two turbines have lower performance even in the median line, confirming the fact that the flows are not fully developed. A comparison with the two-dimensional simulation at the same angle would not be correct because that model has maximum value at an angle of less, as seen in the previous chapter.

Finally, in Fig. 19 the Q field, useful for visualizing vortices (Hunt [32]) of the four model with different Aspect Ratios, is shown. It can be observed how downstream rotor macro-structure swirling changes through different cases. It is also possible to observe that a symmetry of the vortex structures is present in case with AR 1.66, justifying the Cm behavior along height seen above. On contrary, referring to case AR 0.55, a unique structure is detected downstream the turbine, generated by mutual interaction of vortices from upper and lower half. This leads to the fluctuations on torque values, explained above.

6. Conclusions

In this article, a CFD investigation has been conducted on Savonius vertical axis wind turbine. A grid was constructed in order to detect the main flow effect generated by the rotor. In the first part of mesh study, a successive refinement has been done to obtain

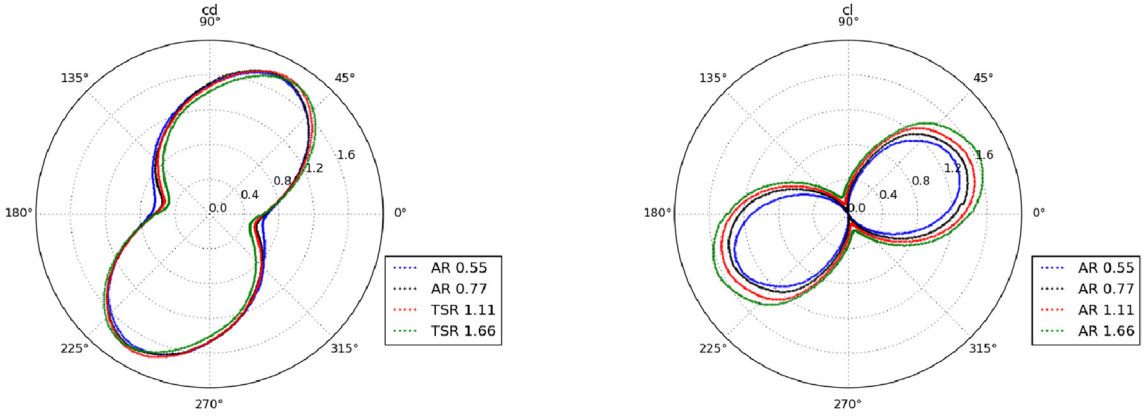

(a) Cd. (b) Cl.

Fig. 16. Polar charts of Drag and Lift coefficient as function of AR.

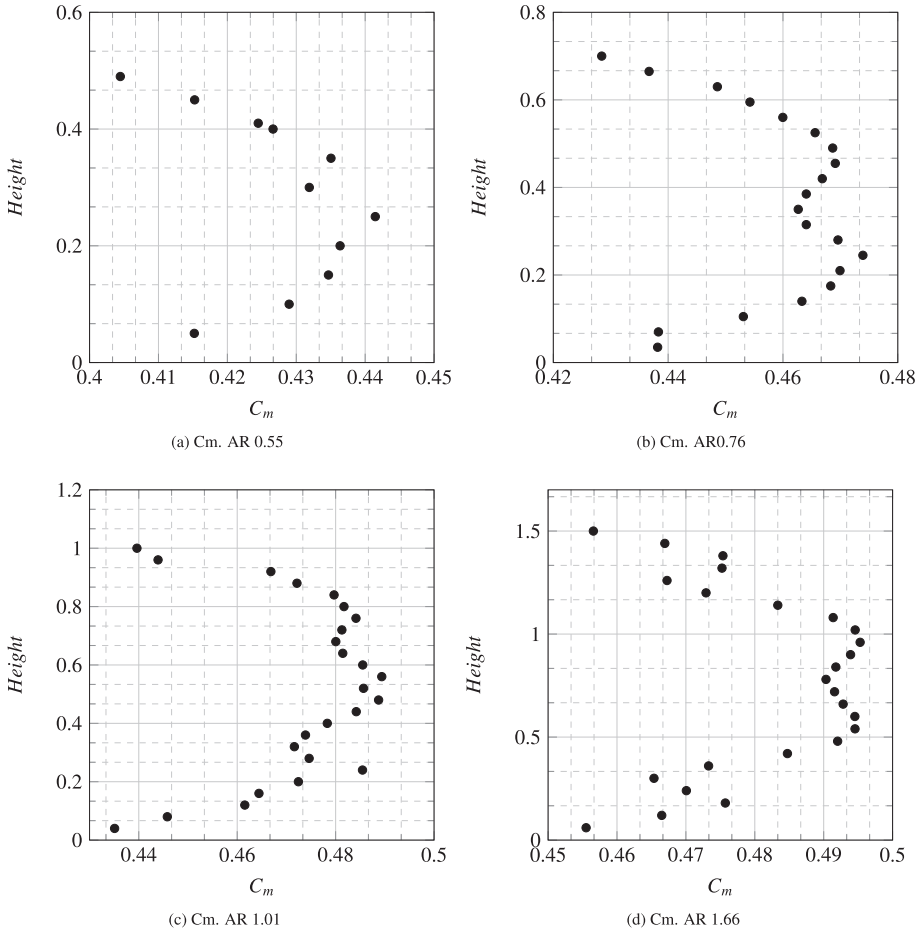

(a) Cm. AR 0.55 (b) Cm. AR0.76

(c) Cm. AR 1.01 (d) Cm. AR 1.66

Fig. 17. Cm along vertical direction for different AR, rotor in position 36°.

performance of the turbine not affected by discretization errors. During the second phase, the optimization has lead to 70% reduction of elements number while maintaining a good accuracy. The 2D model over predict the turbine efficiency and doesn't replicate the shape of characteristic curve. There is a peak shift to TSR 1 while wind tunnel tests report maximum power at TSR 0.8. 3D model has partially solved the problem, reproducing the same characteristic experimental curve but showing a little under-prediction of experimental rotor efficiency. All data are inside uncertainty bands of measurement instruments. This validate the numerical method applied. The last part was focused on rotor height effect over efficiency. A performance improvement was observed for higher rotors but the trend is asymptotic to a limit. Analysing lateral and longitudinal force, the main difference between the rotors has been

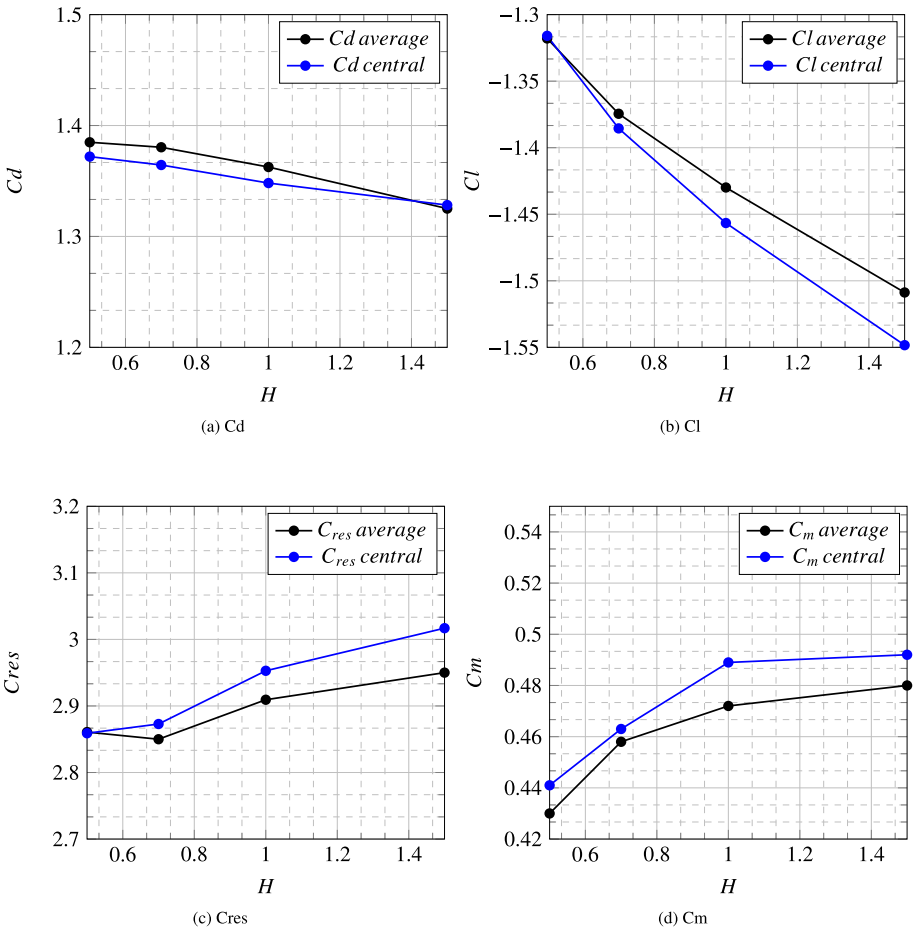

(a) Cd (b) Cl

(c) Cres (d) Cm

Fig. 18. Comparison between mean and median value with rotor in position 36°.

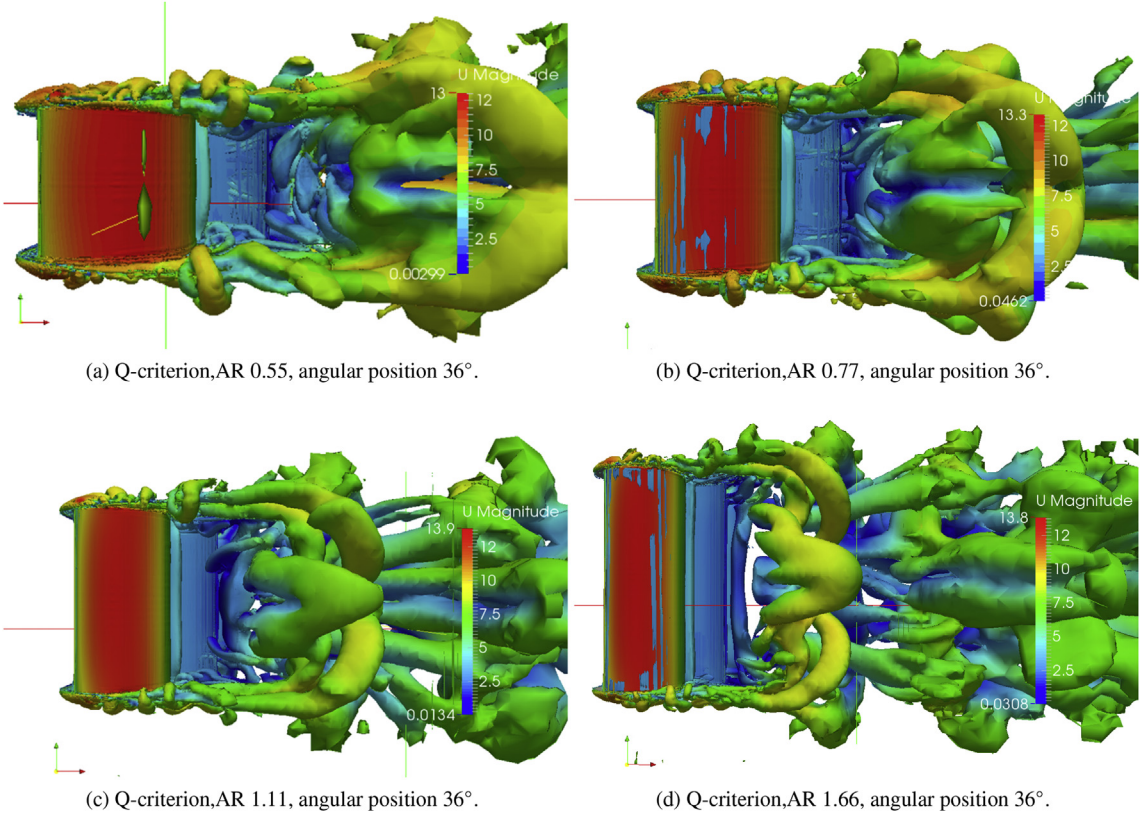

(a) Q-criterion,AR 0.55, angular position 36°.

(b) Q-criterion,AR 0.77, angular position 36°.

(c) Q-criterion,AR 1.11, angular position 36°.

(d) Q-criterion,AR 1.66, angular position 36°.

Fig. 19. Q-criterion at angular position 36°.

observed about lift coefficient. 2D model is characterized by higher lift than the full three-dimensional simulations. In the same way, taller rotors have greater lateral forces on blades.

References

[1] W. E. C.-G, GLOBAL, Global Wind Report: Annual Market Update, GWEC, Brussels, 2014 [Links].

[2] S. J. Savonius, Wind rotor, US patent 1,766,765 (Jun. 24 1930).

[3] M. Kamoji, S. Kedare, S. Prabhu, Experimental investigations on single stage modified savonius rotor, Appl. Energy 86 (7) (2009) 1064–1073.

[4] W. Tian, B. Song, J.H. VanZwieten, P. Pyakurel, Computational fluid dynamics prediction of a modified savonius wind turbine with novel blade shapes, Energies 8 (8) (2015) 7915–7929.

[5] B. Blackwell, R. Sheldahl, L. Feltz, Wind tunnel performance data for two and three bucket savonius rotors, J. Energy 2 (3) (1977) 160–164.

[6] N. Mahmoud, A. El-Haroun, E. Wahba, M. Nasef, An experimental study on improvement of savonius rotor performance, Alexandria Eng. J. 51 (1) (2012) 19–25.

[7] A. Damak, Z. Driss, M. Abid, Performance tests on helical savonius rotors, Renew. Energy 52 (2013) 136–142.

[8] I. Ushiyama, H. Nagai, Optimum design configurations and performance of savonius rotors, Wind Eng. 12 (1) (1988) 59–75.

[9] A. Shigetomi, Y. Murai, Y. Tasaka, Y. Takeda, Interactive flow field around two savonius turbines, Renew. Energy 36 (2) (2011) 536–545.

[10] R.E. Peter, B.S. Lissaman, Applied Aerodynamics of Wind Power Machines, Book, vol. 1, 1974, pp. 1–117.

[11] S. Sivasegaram, Design parameters affecting the performance of resistance-type, vertical-axis windrotors-an experimental investigation, Wind Eng. 1 (1977) 207–217.

[12] S.C. Goh, J.U. Schlüter, Numerical simulation of a savonius turbine above an infinite-width forward facing step, Wind Eng. (2016), 0309524X15624619.

[13] K. Kacprzak, G. Liskiewicz, K. Sobczak, Numerical investigation of conventional and modified savonius wind turbines, Renew. Energy 60 (2013) 578–585.

[14] V. DAlessandro, S. Montelpare, R. Ricci, A. Secchiaroli, Unsteady aerodynamics of a savonius wind rotor: a new computational approach for the simulation of energy performance, Energy 35 (8) (2010) 3349–3363.

[15] J.V. Akwa, G. da Silva Júnior, A. Petry, Discussion on the verification of the overlap ratio influence on performance coefficients of a savonius wind rotor using computational fluid dynamics, Renew. Energy 38 (1) (2012) 141–149.

[16] M. Mohamed, Design Optimization of Savonius and Wells Turbines, Ottovon-Guericke University Magdeburg.

[17] P. Gupta, Stator use influence on the performance of a savonius wind rotor using cfd, Therm. Eng. Res. 10 (1) (2011) p63–72.

[18] C. Kang, H. Liu, X. Yang, Review of fluid dynamics aspects of savonius-rotor-based vertical-axis wind rotors, Renew. Sustain. Energy Rev. 33 (2014) 499–508.

[19] I. Dobrev, F. Massouh, Cfd and piv investigation of unsteady faaaaalow through savonius wind turbine, Energy Proced. 6 (2011) 711–720.

[20] P. Jaohindy, S. McTavish, F. Garde, A. Bastide, An analysis of the transient forces acting on savonius rotors with different aspect ratios, Renew. Energy 55 (2013) 286–295.

[21] S. Roy, U. Saha, Comparative analysis of turbulence models for flow simulation around a vertical axis wind turbine, in: Proceedings of Indo-danish International Conference on Wind Energy: Materials, Engineering, and Policies, November, 2012, pp. 22–23.

[22] T. Krysiński, Z. Buliński, A.J. Nowak, Numerical modeling and preliminary validation of drag-based vertical axis wind turbine, Arch. Thermodyn. 36 (1) (2015) 19–38.

[23] M. Nasef, W. El-Askary, A. AbdEL-Hamid, H. Gad, Evaluation of savonius rotor performance: static and dynamic studies, J. Wind Eng. Ind. Aerodyn. 123 (2013) 1–11.

[24] S. Sivasegaram, Secondary parameters affecting the performance of resistance type vertical axis wind rotors, Wind Eng. 2 (1978) 49–58.

[25] D.C. Wilcox, Turbulence Modeling for CFD, DCW Industries, Inc., La Canada, California, 1988.

[26] P. Spalart, S. Allmaras, A one-equation turbulence model for aerodynamic flows, La Rech. Aerosp. 1 (1994) 5–21.

[27] T.-H. Shih, W.W. Liou, A. Shabbir, Z. Tang, J. Zhu, A new k-epsilon eddy viscosity model for high reynolds number turbulent flows, Comput. Fluids 24 (3) (1995) 227–238.

[28] F.R. Menter, Zonal two equation k-turbulence models for aerodynamic flows, AIAA Pap. 2906 (1993) 1993.

[29] I. Ross, Wind Tunnel Blockage Corrections: an Application to Vertical-axis Wind Turbines, University of Dayton, 2010. Ph.D. thesis.

[30] E. Colombo, F. Inzoli, R. Mereu, A methodology for qualifying industrial cfd: the Q^3 approach and the role of a protocol, Comput. Fluids 54 (2012) 56–66.

[31] Z. Zhao, Y. Zheng, X. Xu, W. Liu, G. Hu, Research on the improvement of the performance of savonius rotor based on numerical study, in: Sustainable Power Generation and Supply, 2009. SUPERGEN'09. International Conference on, IEEE, 2009, pp. 1–6.

[32] J. Hunt, A. Wray, P. Moin, Eddies, Streams, and Convergence Zones in Turbulent Flows, 1988, pp. 193–208. Center for turbulence research report CTR-S88.

Nomenclature

D_t: Diameter of the turbine [m]
D_p: Diameter of the end plate [m]
H: Height of the rotor [m]
P: Power [W]
M: Torque [Nm]
d: Diameter of the blade [m]
s: Thickness of the blade and end plate [m]
AR: Aspect Ratio [−]
o: Distance between the blades [m]
A: Frontal area of the turbine
A_{wt}: Frontal area of the wind tunnel [m^2]
U_{inf}: Free-stream velocity of the wind [m/s]
λ: Blockage factor
ω: Angular velocity [rad/s]
OR: Overlap ratio [−]
ρ: Density of the air [kg/m^2]
ν: Cinematic viscosity [m^2/s]
α: Angle of position of the rotor [°]
C_p: Coefficient of power [−]
C_m: Coefficient of momentum [−]
C_d: Coefficient of drag [−]
C_l: Coefficient of lift [−]
C_{res}: Coefficient of equivalent resistant force [−]
TSR: Tip Speed Ratio [−]
Re: Reynolds number [−]